Aeroacoustics Conferences
June 4-7, 2024, Rome, Italy
30th AIAA/CEAS Aeroacoustics Conference (2024)

10.2514/6.2024-3395

Experimental identification of airfoil stall noise sources in static and dynamic conditions

Lisa Sicard *, Malek Dakhli †
IMSIA, ENSTA Paris, Institut Polytechnique de Paris, France

Romain Monchaux ‡
LMI, UME, ENSTA Paris, Institut Polytechnique de Paris, France

Benjamin Cotté §
IMSIA, ENSTA Paris, Institut Polytechnique de Paris, France

Dynamic stall noise is an important concern in several open rotor applications such as wind turbines. In order to identify the coherent aerodynamic structures responsible for the noise radiation at high angles of attack, a large database of synchronized flow and acoustic measurements have been obtained in an anechoic wind tunnel in both static and dynamic conditions. For a static airfoil at high angle of attack, the velocity fluctuations evaluated from the time-resolved particle image velocimetry data are correlated with acoustic pressure to localize aeroacoustic sources associated with deep stall noise. The noise is strongly linked to the Bénard-von Kármán vortex shedding generated by the interaction of the trailing edge vortex with the Kelvin Helmholtz instability produced in the separation bubble shear layer. For an oscillating airfoil, the reduced frequency is shown to have a significant impact on the flow topology and on the noise radiation. Some distinct features are observed between quasi-static and dynamic stall regimes.

I. Introduction

Wind turbine noise is characterized by amplitude modulations that are a potential cause of annoyance for wind farm neighbors. One of the possible reasons for the occurrence of strong amplitude modulations at large distances is dynamic stall noise, related to the periodic separation and reattachment of the boundary layer on the wind turbine blade suction side during one rotation [1]. This issue can be present on horizontal axis wind turbines, e.g. when the wind shear is strong, and is also significant on vertical axis wind turbines when the tip speed ratio is low [2, 3].

In static conditions, two distinct stall noise regimes have been identified by Moreau et al. [4] when studying the NACA 0012 airfoil self-noise near stall and in stall conditions. Near the stall angle, the authors noted an increase in the amplitude of the noise spectrum over a wide frequency band between 200 Hz and 400 Hz . This corresponds to the light stall noise regime. When the angle of attack further increases and largely exceeds the static stall angle, a second acoustic regime called deep stall noise is identified. The deep stall noise is characterized by a decrease in the amplitude of the broadband noise and the appearance of a narrow band peak around 100 Hz whose amplitude is approximately 10 dB higher than that of the light stall noise. Modeling of airfoil stall noise is still quite limited [4–6], and the mechanisms of stall noise generation are not fully understood. Lacagnina et al. [7] have proposed some explanations for the light stall noise, involving the scattering of hydrodynamic pressure fluctuations by the airfoil trailing edge. These fluctuations can originate from coherent structures or instabilities in the shear layer, or from shear layer flapping. To our knowledge, the mechanisms for deep stall noise radiation have not be detailed in the literature.

In dynamic conditions, noise radiation as well as airfoil aerodynamics strongly depend on the pitching frequency f_0. For small values of f_0, corresponding to the quasi-static regime, unsteady effects are small and the behavior is close to the static regime. On the contrary, a dynamic stall regime is found for high values of f_0. The influence of the oscillation frequency has been studied by Raus et al. [8], who showed that the NACA 0012 airfoil radiation strongly increases with oscillation frequency. In the quasi-static regime, they retrieved the light and deep stall noise regimes observed in static

*PhD student, ENSTA Paris, Institute of Mechanical Sciences and Industrial Applications
†Intern, ENSTA Paris, Institute of Mechanical Sciences and Industrial Applications
‡Associate Professor, ENSTA Paris, LMI, UME
§Associate Professor, ENSTA Paris, Institute of Mechanical Sciences and Industrial Applications, benjamin.cotte@ensta-paris.fr

conditions. However, in the dynamic stall regime, new features were observed, related to the presence of a dynamic stall vortex and to delayed flow separation and reattachement, as also noticed by Mayer et al. [9]. To our knowledge, only one study has attempted to identify the coherent structures that contribute to sound emission in dynamic conditions [10], and a better understanding of the dynamic stall noise sources is needed to develop models and mitigation techniques associated to this phenomenon.

The objective of this paper is thus to identify and localize the aerodynamic noise sources for an airfoil at high angles of attack in static and dynamic conditions using synchronous flow and acoustic measurements. This is done by characterizing the airfoil noise spectra, by studying the flow topology using vorticity fields and the Γ_2 criterion for vortex detection, and by cross-correlating the velocity fluctuations around the airfoil and the far-field acoustic pressure. The airfoil under study is a thick and cambered NACA 63_3418 airfoil that is typically used on the tip region of wind turbine blades.

II. Experimental setup

The experiment is performed in the anechoic wind tunnel of the École Centrale de Lyon. The anechoic wind tunnel is composed of an anechoic chamber of $8 \times 9 \times 10\,\mathrm{m}^3$ including a rectangular subsonic jet exit of $0.4 \times 0.3\,\mathrm{m}^2$ and a semi-open test section with two horizontal end plates guiding the incident flow at the jet exit, see Figure 1. The measurements are performed for a NACA 63_3418 airfoil with a chord $c = 0.12\,\mathrm{m}$ and a span $s = 0.30\,\mathrm{m}$. The airfoil is placed vertically between the end plates by means of discs allowing the profile rotation around its chord center, the upper disc being glass to allow the visualization of the flow. A horizontal plane (x, y) is defined at mid-span of the airfoil and centered on the airfoil chord center with the x-axis defined parallel to and of the same direction as the incident flow. The airfoil is subjected to an inflow velocity $U_\infty = 50\,\mathrm{m/s}$, corresponding to a chord based Reynolds number $Re_c = U_\infty\, c/\nu = 4 \times 10^5$, and a Mach number $M_a = U_\infty/a = 0.15$, with ν and a representing respectively the kinematic viscosity of the flow and the sound speed, estimated for a ambient temperature of 283.15 K. The residual turbulence rate of the wind tunnel is measured at 0.4%. To trigger the turbulent boundary layer transition, a 5 mm wide tripping tape is placed on the airfoil pressure side near the leading edge at $x/c = -0.4$ along the span. This zigzag tripping prevents the formation of the Tollmien-Schlichting waves at the origin of laminar boundary layer noise which can interfere with the acoustic stall regimes identification at low Reynolds numbers.

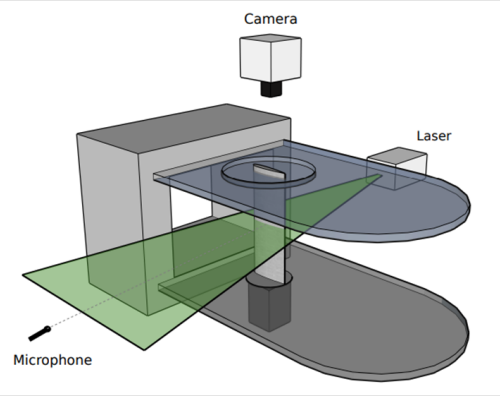

Fig. 1 Experimental Set Up in the anechoic wind tunnel of the École Centrale de Lyon. The flow from left to right.

In static conditions, the airfoil is placed at various angles of attack α_g between 0° and 30°, as shown in Table 1. To compensate the effect of jet deflection associated with the open-jet wind tunnel, Garner's correction [11] is used to calculate effective angles of attack α_e, see Table 1. Further details on these corrections implementation in our setup can be found in Raus *et al.* [8]. In dynamic conditions, the airfoil is subjected to a sinusoidal pitching motion about its center chord:

$$\alpha_g = \alpha_0 + \alpha_A \sin(2\pi f_0 t), \tag{1}$$

where f_0 is the oscillation frequency and $\alpha_0 = \alpha_A = 15°$. No effective angle is calculated in dynamic conditions, as Garner correction has not been tested for an oscillating airfoil. Three reduced frequencies are tested $k = 0.01$, $k = 0.025$

and $k = 0.05$ with $k = \pi f_0 c/U_\infty$. Parameters associated with the experiments are given in Table 2. Sheng *et al.* [12] define the reduced pitch rate as $k_\star = \alpha_A k$ and estimate the boundary between quasi-static and dynamic stall at $k_\star = 0.01$ for NACA airfoils. As a result, unsteady effects associated with dynamic stall are expected to be significant for the highest oscillation frequency tested in the experimental campaign.

α_g (°)	0	15	18	27	30
α_e (°)	-0.6	10.2	13.4	23.8	26.3

Table 1 Correspondence between the geometric angles of attack α_g and the effective angles α_e calculated with the Garner et al. [11] correction.

f_o (Hz)	k	$k_\star$	N_{runs}	N_{cycles}	$N_{samples}$
0.660	0.005	1.3×10^{-3}	20	1.1	4540
1.326	0.01	2.6×10^{-3}	10	2.2	2262
3.316	0.025	6.5×10^{-3}	5	5.5	905
6.60	0.05	13×10^{-3}	2	10.9	454

Table 2 Oscillation frequencies f_0, reduced frequency k, reduced pitch rate $k_\star$, number of PIV runs N_{runs}, number of cycles per run N_{cycles}, and number of samples per cycle $N_{samples}$.

The velocity fields are measured using a two-dimensional Time-Resolved Particle Image Velocimetry (2D TR-PIV) system in the horizontal plane (x, y) on the airfoil suction side, as shown in Figure 1, with u' and v' the associated velocity fluctuations components. A Phantom VEO1310 camera is positioned above the upper guiding disc. Velocity field measurements are performed ten times independently in a 166.8×222 mm^2 field of view with a spatial resolution of 5.76 px/mm. The TR-PIV sampling frequency is $f_{PIV} = 3$ kHz with an acquisition duration of 1.65 s, thus 4953 images are recorded for each acquisition. The particles are illuminated at 532 nm by a dual pulse laser, the Mesa PIV 532-120-M from Amplitude Laser® delivering 9 mJ per pulse, connected to an articulated arm. Data acquisition and processing are performed with the Lavision's Davis 10.1.2 software. A data preprocessing including a temporal filtering and a masking of the shadow zones is applied. Velocity vector fields are computed with a multi-pass cross-correlation algorithm with a final interrogation window size of 16×16 px^2 and an overlap of 50%. Selection criteria based on peak ratio and residual threshold values are applied in post-processing to eliminate spurious vectors.

Far-field acoustic measurements are performed using a Gras 46 BE microphone placed 2 m from the airfoil center in the mid-span plane. The microphone is facing the airfoil pressure side and is directed perpendicular to the test section, as shown in figure 1. The acoustic sampling frequency is $f_a = 51.2$ kHz. The acoustic measurements are synchronized with 2D TR-PIV measurements, and the acquisition time is chosen equal to 2 seconds. It is longer than the TR-PIV acquisition time set to 1.65 s to take into account the acoustic propagation time that is close to 6 ms. For each angle of attack in static conditions, the synchronized flow and acoustic measurements are carried ten times independently. For each oscillation frequency in dynamic conditions, several runs are also measured in order to have at least 20 complete cycles, as shown in Table 2. Since the number of cycles N_{cycles} during the PIV acquisition time varies between 1 and 10 when f_0 increases from 0.66 Hz to 6.6 Hz, 2 runs are performed for the highest frequency while 20 runs are needed at the lowest frequency. In order to perform phase-averaging over a large number of cycles, additional acoustic measurements are also performed over 100 cycles without flow measurements. Finally, background noise measurements are performed over a period of 30 s to characterize the noise generated by the wind tunnel, end plates and measuring devices.

III. Results in static conditions

A. Characterization of airfoil noise spectra and flow topology

Let us first compare the acoustic signatures measured at different effective angles of attack α_e. The power spectral densities (PSD) of the acoustic pressure S_{pp} averaged over the ten acquisition runs are plotted in Figure 2 for five angles of attack and for the background noise. As the background noise is dominant for frequencies below 70 Hz, the acoustic analysis is restriced to frequencies between 70 Hz and 1500 Hz. First, at zero incidence, the signal to noise ratio is low, with a broadband noise radiation emerging above 600 Hz. This corresponds to trailing edge noise associated with an attached turbulent boundary layer. At the higher angles of attack $\alpha_e = 10.2°$ and at $\alpha_e = 13.4°$, the noise radiation increases significantly between 400 Hz and 1000 Hz. This is characteristic of the light stall noise [4]. At the highest angle of attack of $\alpha_e = 26.3°$, a narrow-band peak of high amplitude around 162 Hz appears, which is a typical feature of the deep stall noise [4]. The noise radiation at $\alpha_e = 23.8°$ shows an intermediate behavior, with a decrease in the amplitude of the light stall noise and the appearance of a broadband hump around 240 Hz. Raus *et al.* [13] have shown that the boundary layer separation point gradually moves from the trailing edge to the leading edge between $\alpha_e = 10.2°$ and $\alpha_e = 23.8°$, which is consistent with these noise radiation behaviors.

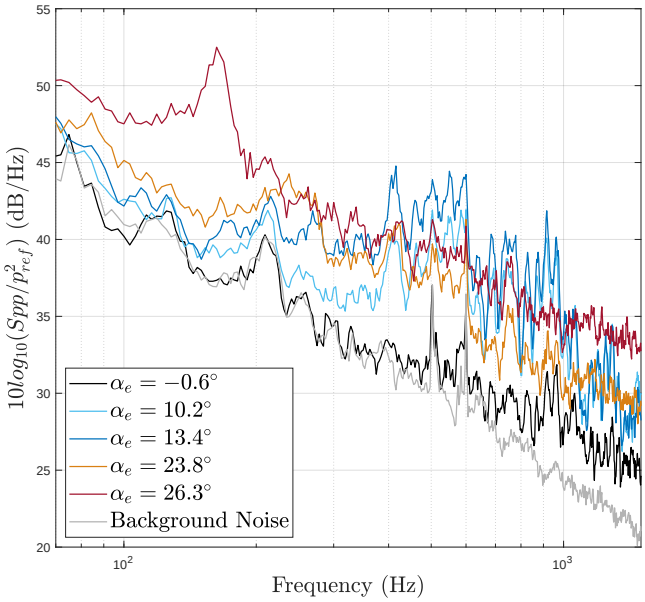

Fig. 2 PSD of far-field sound pressure for different angles of attack averaged over the ten independent runs.

Let us now focus on the deep stall noise regime at $\alpha_e = 26.3°$. In order to visualize the mean flow topology, the ensemble-averaged streamlines are plotted in Figure 3, along with two components of the Reynolds tensor. The flow is completely separated from the leading edge on the airfoil suction side. The wake presents two recirculation zones. The first one is bounded by the leading edge shear layer and is associated to a separation bubble reattaching to the trailing edge. The second one is located near the trailing edge and results from the interaction of the separation bubble with the flow coming from the pressure side of the airfoil. Both recirculation zones have opposite circulation. If the latter is small, the former is too long to fit in the PIV field of view. Nevertheless, its length can be estimated to be of the same order of magnitude as the airfoil chord. The Reynolds stress distributions highlight the presence of high turbulent activity in the shear layers starting at the leading and trailing edges.

As turbulent coherent structures play an important role in the noise produced by a flow, we seek to identify the turbulent structures present in the wake at $\alpha_e = 26.3°$. This identification is performed using the Eulerian vortex detection criterion Γ_2. This criterion intoduced by Graftieaux et al. [14] involves a scalar function that varies within the range of -1 to 1, with its extrema highlighting the spatial position of vortices center. Positive values indicate the presence of a vortex rotating clockwise, while negative values indicate the presence of a vortex rotating counterclockwise.

Figures 4(a) and (b) show the spatial distribution of the percentage of time associated with positive and negative

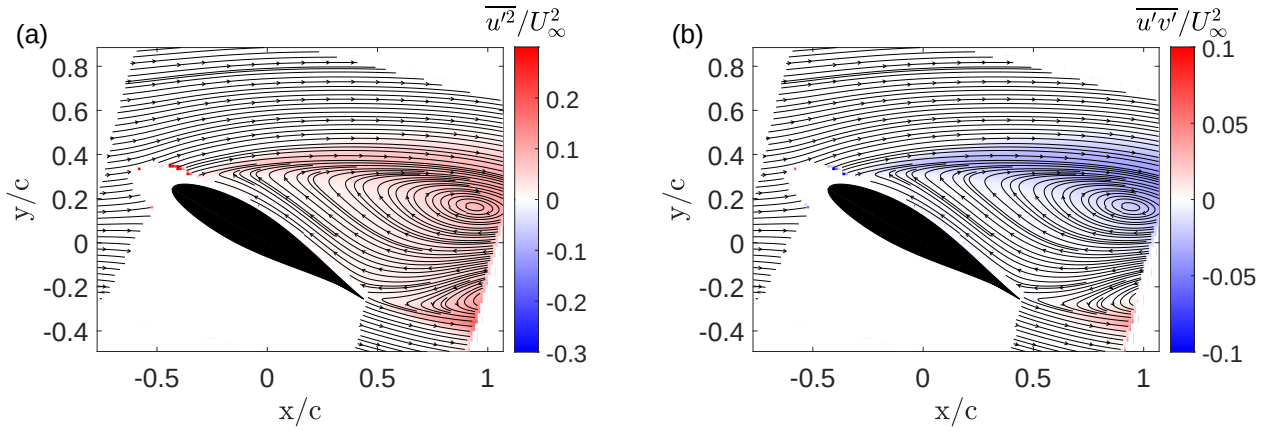

(a) (b)

Fig. 3 Streamlines of the mean flow with (a) the $\overline{u'^2}$ component of the Reynolds tensor and (b) the $\overline{u'v'}$ component of the Reynolds tensor averaged over the ten independent runs at $\alpha = 26.3°$.

vortices respectively. A threshold of ± 0.85 is used and the integration area includes 3×3 PIV points, following Mulleners and Raffel [15]. We observe in Figures 4(a) clockwise-rotating vortices that are recurrently identified over time, that suggests the presence of a Kelvin-Helmholtz instability. On the other hand, Figures 4(a) shows the presence of counterclockwise-rotating vortex centers in the trailing edge shear layer, corresponding to a large-scale trailing edge vortex.

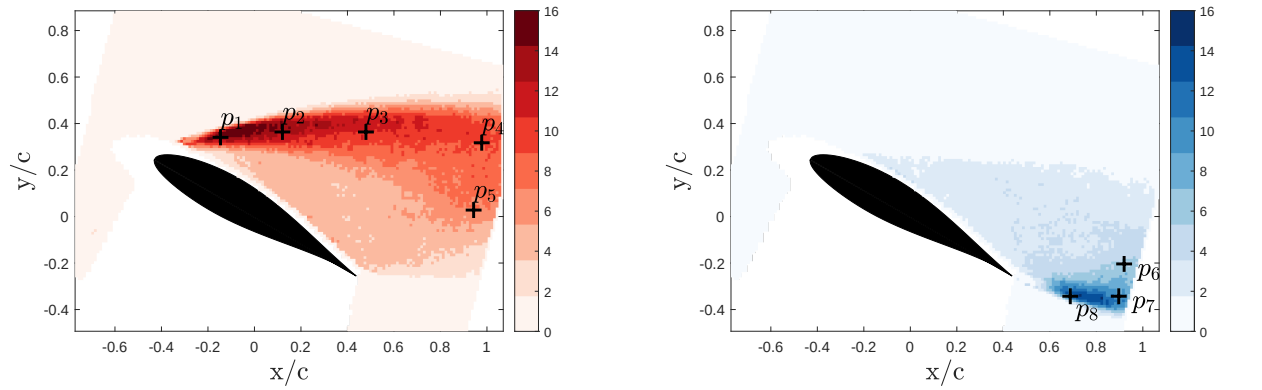

(a) (b)

Fig. 4 Spatial distribution of the percentage of time spent by Γ_2 in (a) positive values greater than a threshold of 0.85 and (b) negative values lower than a threshold of -0.85 during a data acquisition for an integration area comprising 3×3 PIV points for $\alpha_e = 26.3°$

B. Identification of acoustic sources in deep stall conditions

In order to localize the acoustic sources in the flow, we now calculate the normalized cross-correlations between the velocity fluctuations u' or v' and the acoustic pressure p:

$$R_{\mathrm{u'p}}(\underline{x},\tau) = \frac{1}{N_t}\frac{\sum_{i=1}^{N_t} u'\left(\underline{x},t_i\right) p\left(t_i-\tau\right)}{\sigma(u')\sigma(p)}, \tag{2}$$

$$R_{\mathrm{v'p}}(\underline{x},\tau) = \frac{1}{N_t}\frac{\sum_{i=1}^{N_t} v'\left(\underline{x},t_i\right) p\left(t_i-\tau\right)}{\sigma(v')\sigma(p)}, \tag{3}$$

with $\sigma(X)$ the standard deviation of X. Figures 5(a) and (b) show the maximum cross-correlation coefficients obtained at each point in space for the longitudinal and transverse fluctuations over all the correlation delay τ for one run at $\alpha_{\mathrm{e}} = 26.3^{\circ}$ respectively. The maxima of the cross correlations for the two velocity components are located in two different zone downstream of the trailing edge, highlighted by a white rectangle.

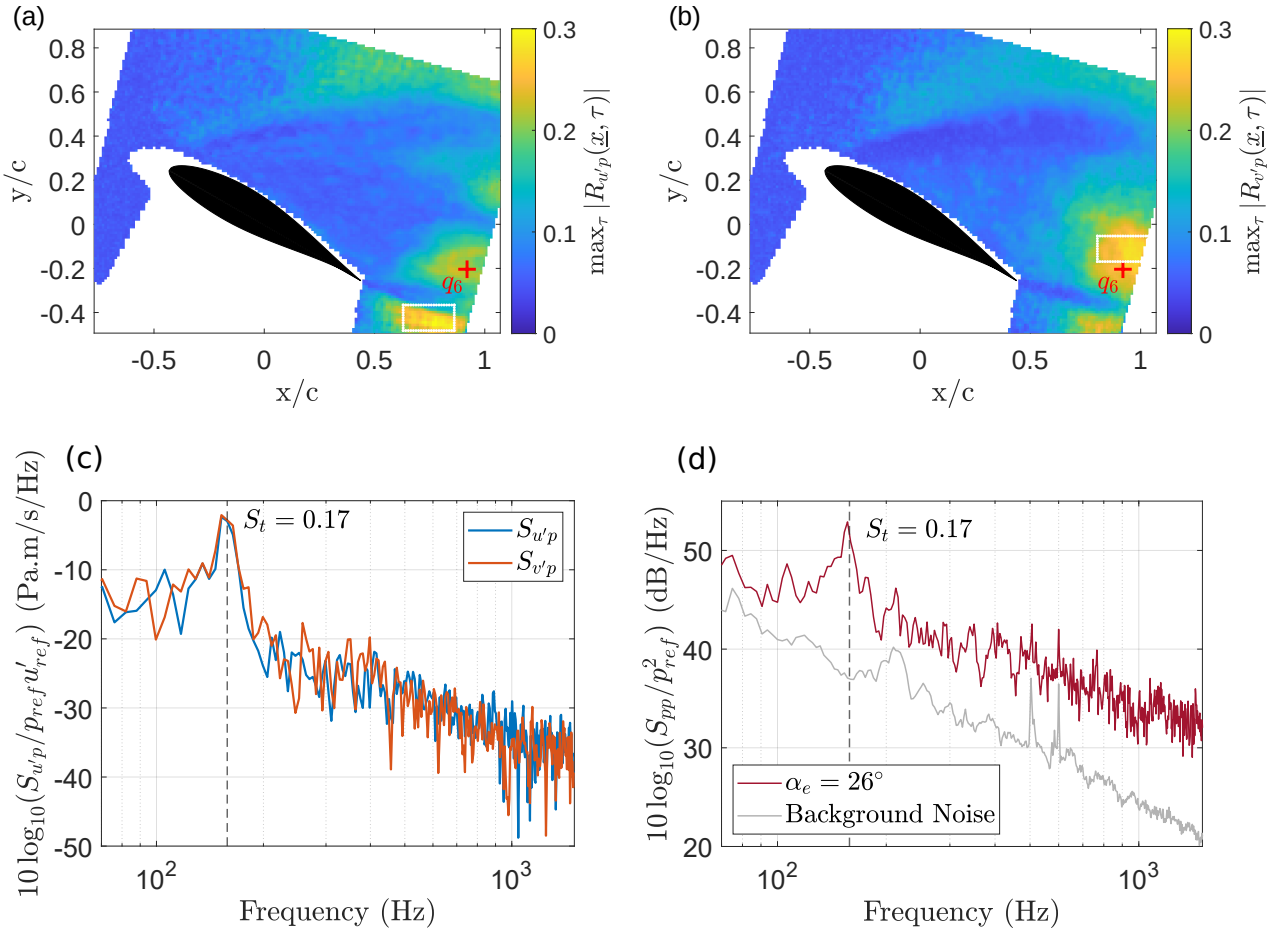

Fig. 5 Top: Map of local maxima over τ of normalised correlations for longitudinal velocity fluctuations (a) and transverse velocity fluctuations (b) for one acquisition run. Bottom: (c) Local average of the CPSDs computed in the maximum correlation zone and (d) PSD of far-field acoustic pressure.

In order to obtain more information about these correlations, we calculate the cross power spectral density (CPSD) $\overline{S_{\mathrm{u'p}}}$ and $\overline{S_{\mathrm{v'p}}}$ between the velocity fluctuations u' and v', respectively, and the acoustic pressure for the points located in the white rectangles that contain 10×20 points centered around the spatial maximum of the correlation maps. The local average of the CPSDs $\overline{S_{\mathrm{u'p}}}$ and $\overline{S_{\mathrm{v'p}}}$ are plotted in Figure 5(c), and the PSD of the acoustic pressure is plotted in

Figure 5(d). Note that the spectrum plotted in Figure 5(d) is slightly different from the one plotted in Figure 2 as it is calculated over a single run. It appears that both $\overline{S_{u'p}}$ and $\overline{S_{v'p}}$ contain the same amplitude peak at a frequency of 158 Hz, that is also present in the acoustic spectrum of Figure 5(d). This peak frequency corresponds to a projected Strouhal number $St = fc\sin\alpha_e/U$ of 0.17, close to the typical values corresponding to the bluff body Bénard-von Kármán vortex shedding. Thus, at high angles of attack, the NACA 63_3418 airfoil behaves like a bluff body, and deep stall noise is strongly linked to a structure oscillating around a Strouhal number of 0.17, located downstream of the trailing edge in the airfoil wake.

IV. Results in dynamic conditions

A. Time-frequency analysis of the acoustic signals

In this section, we consider the noise radiated by the oscillating airfoil. The analysis is first performed over 100 oscillation periods for various reduced frequencies k. This allows us to calculate phase-averaged spectrograms over a large number of cycles, as shown in Figure 6. Spectrograms are computed using a short-term Fourier transform with 80% overlap with various window sizes that yield time resolutions of 14 ms, 6 ms and 3 ms respectively. The results are similar to the ones obtained by Raus *et al.* [13] using an instrumented NACA $63_3 - 418$ airfoil. The main difference is that the motor noise issues that contaminated the acoustic results at high oscillating frequencies in Raus *et al.* [13] have now been solved.

For the reduced frequency $k = 0.01$, corresponding to the quasi-static regime, we retrieve the same acoustic regimes as in Figure 2 in static conditions. The noise levels are low for small angles of attack, and a broadband radiation between 400 Hz and 1000 Hz emerges when the angle of attack exceeds approximately 15°, corresponding to the light stall noise. This pattern is also retrieved during the descending phase. Close to the maximum angle of attack of 30°, a spectral peak close to 160 Hz is clearly present, corresponding to the deep stall noise. In-between these two regimes, a broadband noise radiation is present, that can probably be related to the complete boundary layer detachment and reattachment. Note that the spectrogram at the lowest reduced frequency of $k = 0.005$ (not shown here) is similar to the one at $k = 0.01$.

For the highest reduced frequency $k = 0.05$, corresponding to the dynamic regime, it is more difficult to distinguish the different phases. This can be due to a more complex flow topology, but also to the fact that a small number of samples are used in each block of the short-term Fourier transform in order to obtain a small enough time resolution, which means that the frequency resolution is degraded. In any case, it is clear that the radiated noise levels are significantly stronger in this regime compared to the quasi-static regime. For the intermediate reduced frequency $k = 0.025$, the pattern is closer to the quasi-static regime, with noise levels that are in-between the two extreme cases.

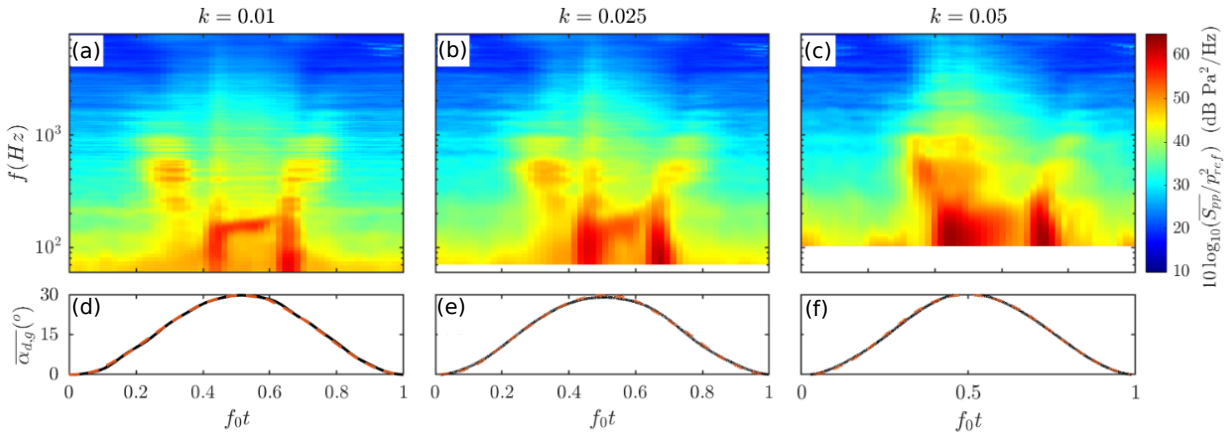

Fig. 6 (a-b-c) Phase-averaged spectrograms of far-field acoustic pressure and (d-e-f) phase-averaged angle of attack for three reduced frequencies k. The overbar denotes phase-averaging.

B. Phase-averaged vorticity

In static conditions, we have identified that the turbulent structures in the wake of the airfoil, linked to the interaction between the shear layers emanating from the leading edge and the trailing edge, are associated to the radiated noise. In order to visualize the evolution of these shear layers during the airfoil oscillation in dynamic conditions, each oscillation is divided into 20 segments, and the vorticity field is phased-averaged using all available runs.

Figure 7 shows the phase-averaged normalized vorticity $\omega c/U_\infty$ for the 12 segments with the highest angle of attack for the lowest oscillation frequency ($k = 0.005$). We observe that the shear layer with positive vorticity remains close to the airfoil suction side up to $\overline{\alpha} = 17.3°$. Above this angle the flow separation becomes more important, until the separation point reaches the leading for $\overline{\alpha} = 29.7°$, close to the highest incidence angle. During the descending motion, the shear layer reattaches around $\overline{\alpha} = 17.5°$. Although this case is considered as quasi-static, an hysteresis can be clearly seen by comparing the vorticity fields around 25.5° or 28.3° in ascending and descending motion.

To visualize the effect of the oscillation frequency on the flow topology, Figures 8 and 9 compare respectively the normalized vorticity fields between three reduced frequencies for the 4 segments with the highest angles of attack during the ascending and descending motion of the airfoil. The increase of the reduced frequency is associated with a stall delay. Also, for the some segments such as the one in Figure 9(b), the shear layer seems to oscillate between two states.

To complement this analysis, instantaneous flow visualizations have been produced that include the Γ_2 criterion for vortex detection. The movies for $k = 0.025$ and 0.05 exhibit large-scale structures that seem to correspond to dynamic stall vortices. These movies will be shown at the conference.

V. Conclusion and perspectives

In this paper, we have proposed a methodology to identify the flow structures at the origin of airfoil stall noise. The method has been applied in static conditions to study the deep stall noise of a NACA $63_3 - 418$ airfoil. It has been shown that the peak frequency in the noise spectrum is related to flow structures downstream the trailing edge in the airfoil wake associated to the Bénard-von Kármán vortex shedding.

For an oscillating airfoil, the phase-averaged spectrograms of acoustic pressure show a modification of the noise radiation when the reduced frequency. The phase-averaged vorticity fields also exhibit some differences between the different oscillation frequencies, with a delay of flow separation as k increases.

The next step in this work consists in identifying more precisely the turbulent structures at the origin of dynamic stall noise by performing a cross-correlation analysis between the velocity fluctuations and the acoustic pressure during different phases of the oscillation cycle.

Acknowledgments

This research is funded by the French National Agency for Research under grant agreement N°ANR-18-CE04-0011. We would like to thank Emmanuel Jondeau, Pascal Souchotte and Michel Roger from École Centrale de Lyon for the elaboration and maintenance of the experiment and for fruitful discussion on the data analysis.

References

[1] Oerlemans, S., "Effect of Wind Shear on Amplitude Modulation of Wind Turbine Noise," *International Journal of Aeroacoustics*, Vol. 14, No. 5-6, 2015, pp. 715–728. https://doi.org/10.1260/1475-472X.14.5-6.715, URL http://journals.sagepub.com/doi/10.1260/1475-472X.14.5-6.715.

[2] Weber, J., Becker, S., Scheit, C., Grabinger, J., and Kaltenbacher, M., "Aeroacoustics of Darrieus wind turbine," *International Journal of Aeroacoustics*, 2015. https://doi.org/10.1260/1475-472X.14.5-6.883.

[3] Venkatraman, K., Moreau, S., Christophe, J., and Schram, C., "Numerical investigation of H-Darrieus wind turbine aerodynamics at different tip speed ratios," *International Journal of Numerical Methods for Heat and Fluid Flow*, 2023. https://doi.org/10.1108/HFF-09-2022-0562.

[4] Moreau, S., Roger, M., and Christophe, J., "Flow Features and Self-Noise of Airfoils Near Stall or in Stall," *15th AIAA/CEAS Aeroacoustics Conference (30th AIAA Aeroacoustics Conference)*, American Institute of Aeronautics and Astronautics, Miami, Florida, 2009. https://doi.org/10.2514/6.2009-3198, URL https://arc.aiaa.org/doi/10.2514/6.2009-3198.

[5] Bertagnolio, F., Madsen, H. A., Fischer, A., and Bak, C., "A semi-empirical airfoil stall noise model based on surface pressure measurements," *Journal of Sound and Vibration*, Vol. 387, 2017, pp. 127–162. https://doi.org/10.1016/j.jsv.2016.09.033, URL https://linkinghub.elsevier.com/retrieve/pii/S0022460X16304989.

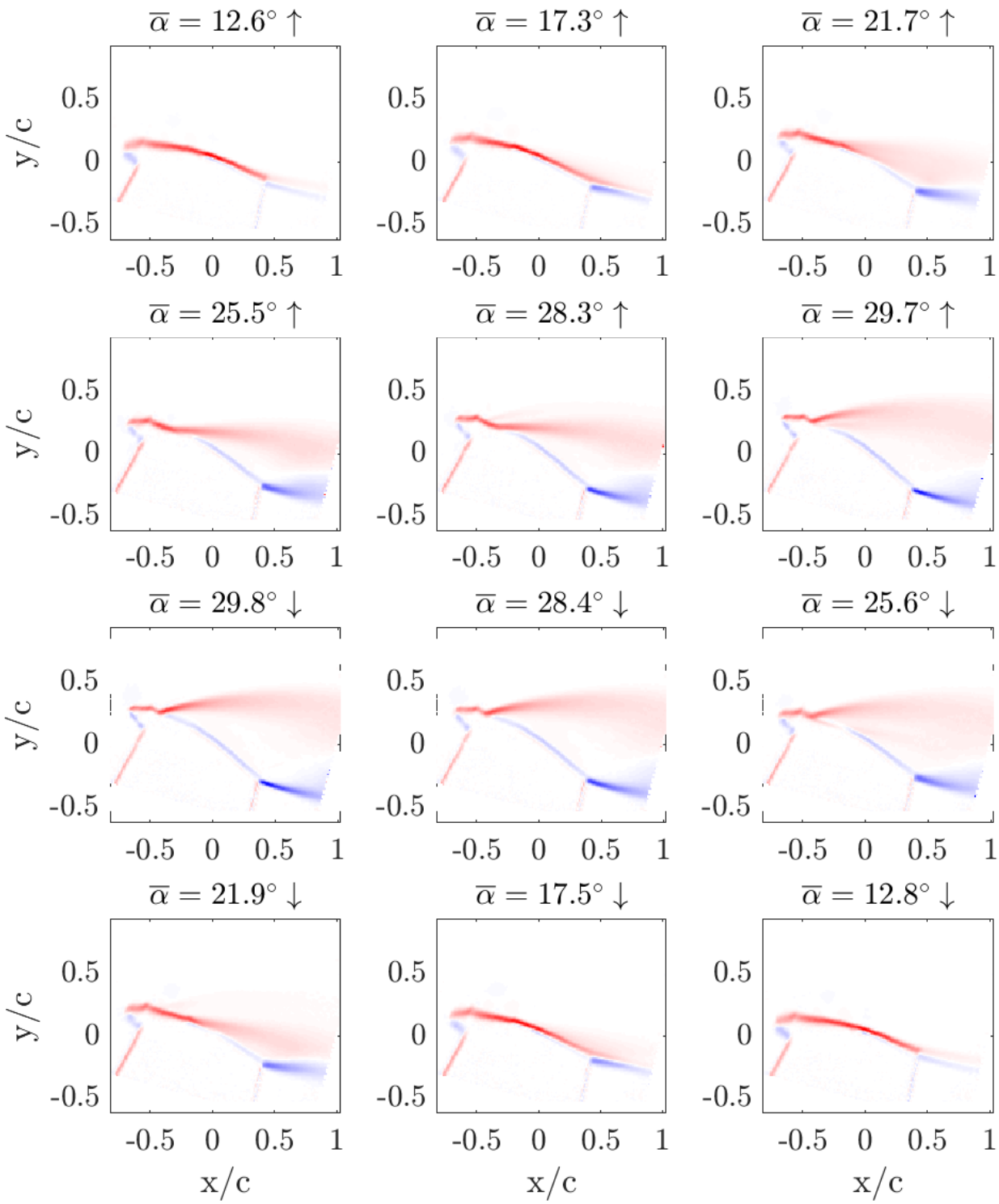

Fig. 7 Phase-averaged normalized vorticity $\omega c/U_\infty$ for various segments at $k = 0.005$. The colorbar is between -0.05 and 0.05.

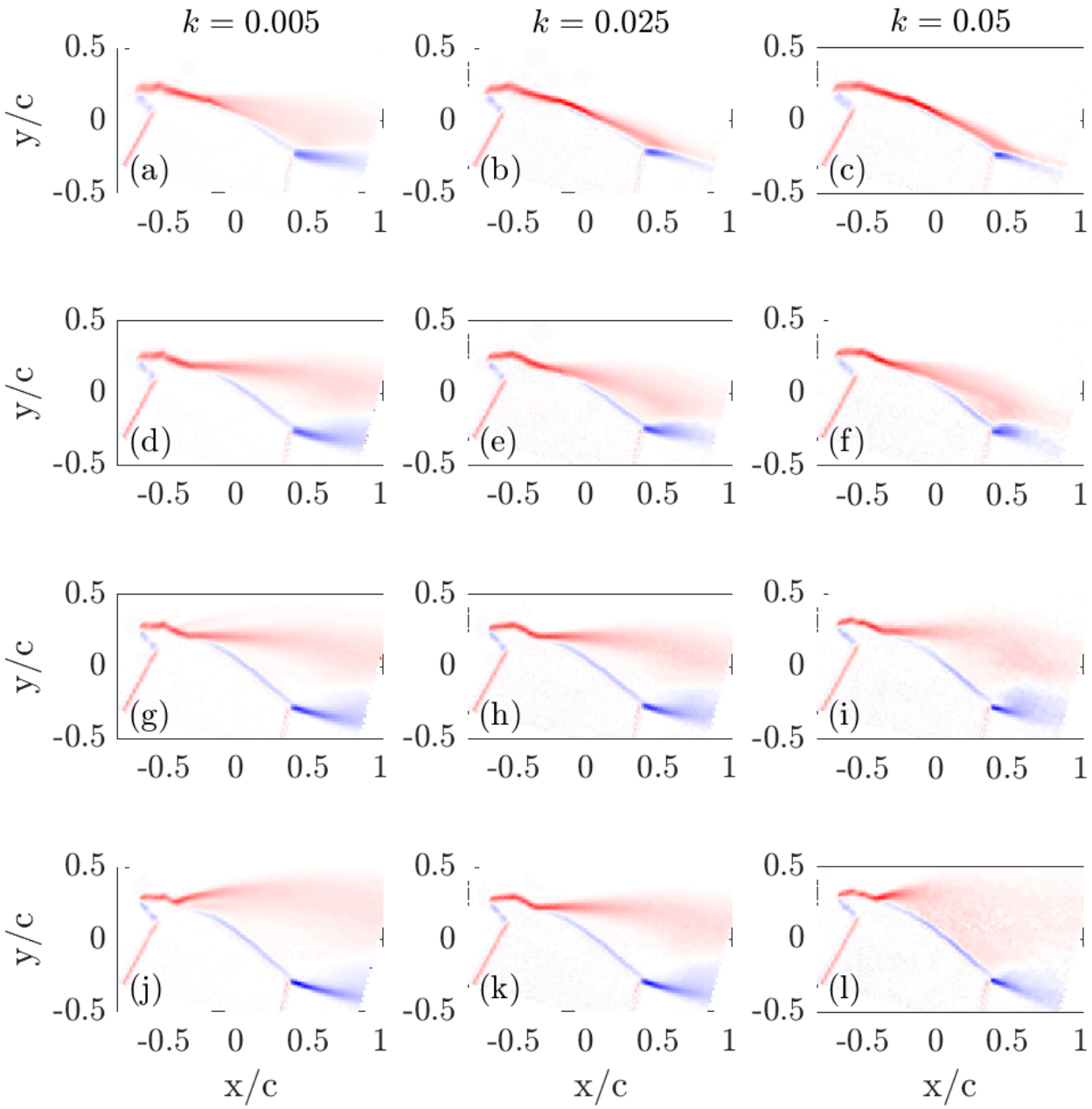

Fig. 8 Phase-averaged normalized vorticity $\omega c/U_\infty$ for the reduced frequencies $k = 0.005$, $k = 0.025$ and $k = 0.05$ for 4 different segments during the ascending motion of the airfoil: (a-c) $\overline{\alpha} \approx 21.7°$, (d-f) $\overline{\alpha} \approx 25.5°$, (g-i) $\overline{\alpha} \approx 28.3°$, (j-l) $\overline{\alpha} \approx 29.7°$. The colorbar is between -0.05 and 0.05.

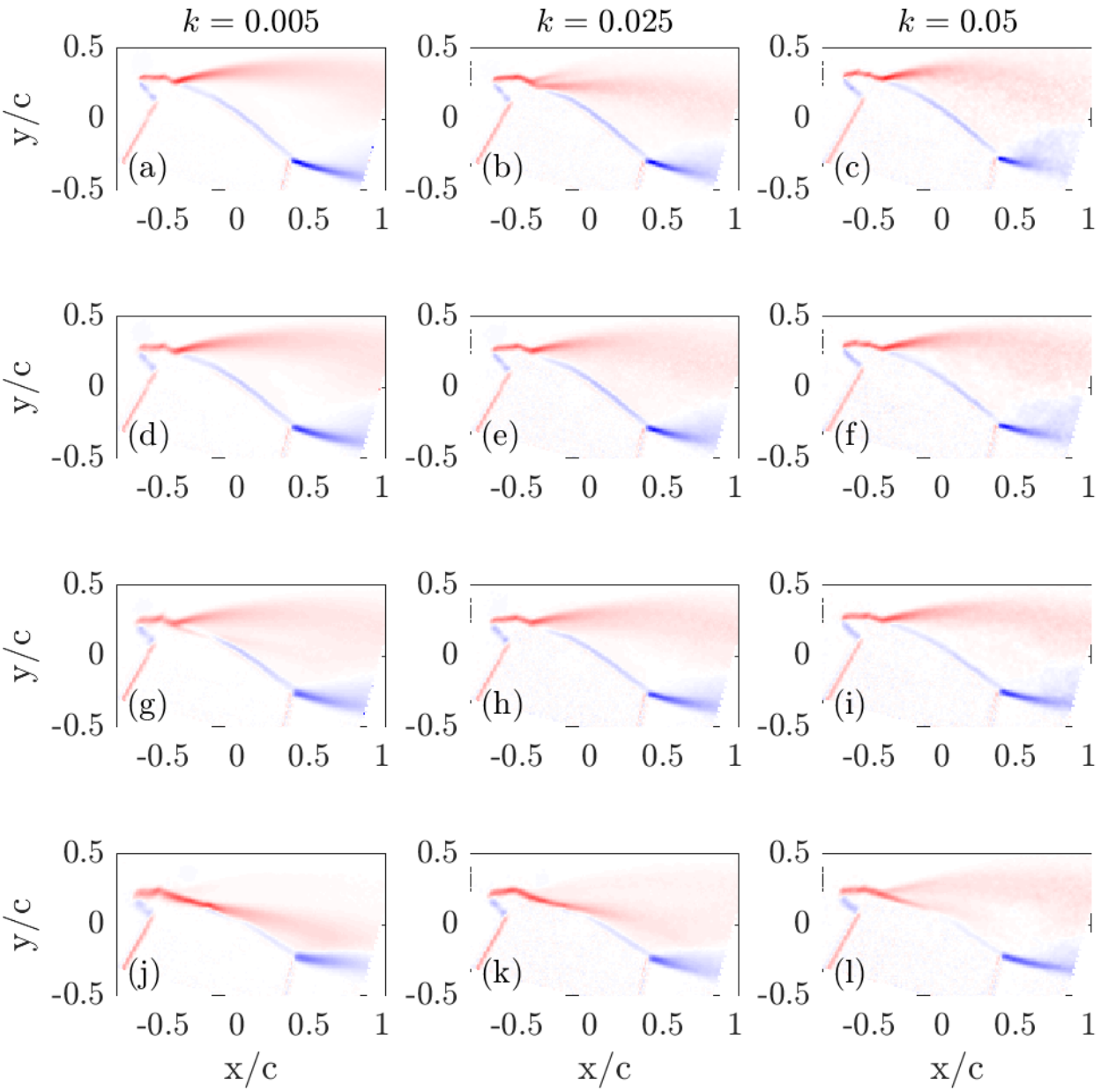

Fig. 9 Phase-averaged normalized vorticity $\omega c/U_\infty$ for the reduced frequencies $k = 0.005$, $k = 0.025$ and $k = 0.05$ for 4 different segments during the descending motion of the airfoil: (a-c) $\overline{\alpha} \approx 29.8°$, (d-f) $\overline{\alpha} \approx 28.4°$, (g-i) $\overline{\alpha} \approx 25.6°$, (j-l) $\overline{\alpha} \approx 21.9°$. The colorbar is between -0.05 and 0.05.

[6] Cotté, B., Roy, S., Raus, D., and Oueini, R., "Towards a semi-empirical trailing edge noise model valid for attached and separated turbulent boundary layers," *28th AIAA/CEAS Aeroacoustics Conference*, 2022, p. 3103.

[7] Lacagnina, G., Chaitanya, P., Berk, T., Kim, J.-H., Joseph, P., Ganapathisubramani, B., Hasheminejad, S. M., Chong, T. P., Stalnov, O., Choi, K.-S., Shahab, M. F., Omidyeganeh, M., and Pinelli, A., "Mechanisms of airfoil noise near stall conditions," *Physical Review Fluids*, Vol. 4, No. 12, 2019, p. 123902. https://doi.org/10.1103/PhysRevFluids.4.123902, URL https://link.aps.org/doi/10.1103/PhysRevFluids.4.123902.

[8] Raus, D., Cotté, B., Monchaux, R., Jondeau, E., Souchotte, P., and Roger, M., "Experimental study of the dynamic stall noise on an oscillating airfoil," *Journal of Sound and Vibration*, Vol. 537, 2022, p. 117144.

[9] Mayer, Y., Zang, B., and Azarpeyvand, M., "Aeroacoustic investigation of an oscillating airfoil in the pre- and post-stall regime," *Aerospace Science and Technology*, Vol. 103, No. 105880, 2020. https://doi.org/10.1016/j.ast.2020.105880.

[10] Siegel, L., Ehrenfried, K., Wagner, C., Mulleners, K., and Henning, A., "Cross-correlation analysis of synchronized PIV and microphone measurements of an oscillating airfoil," *Journal of Visualization*, Vol. 21, 2018, pp. 381–395.

[11] Garner, H. C., Rogers, E., Acum, W., and Maskell, E., "Subsonic wind tunnel wall corrections," Tech. Rep. AD657092, Advisory group aerospace research and development, 1966.

[12] Sheng, W., Galbraith, R., and Coton, F., "Prediction of dynamic stall onset for oscillatory low-speed airfoils," *Journal of Fluids Engineering*, Vol. 130, No. 10, 2008.

[13] Raus, D., Cotté, B., Monchaux, R., Sicard, L., Jondeau, E., Souchotte, P., and Roger, M., "Experimental characterization of the noise generated by an airfoil oscillating above stall," *AIAA AVIATION 2021 FORUM*, 2021, p. 2291.

[14] Graftieaux, L., Michard, M., and Grosjean, N., "Combining PIV, POD and vortex identification algorithms for the study of unsteady turbulent swirling flows," *Measurement Science and technology*, Vol. 12, No. 9, 2001, p. 1422.

[15] Mulleners, K., and Raffel, M., "The onset of dynamic stall revisited," *Experiments in fluids*, Vol. 52, 2012, pp. 779–793.